

# Northumbria Research Link

Citation: Zhang, Qian, Wang, Yong, Wang, Tao, Li, Dongsheng, Xie, Jin, Torun, Hamdi and Fu, Richard (Yongqing) (2021) Piezoelectric Smart Patch Operated with Machine Learning Algorithms for Effective Detection and Elimination of Condensation. ACS Sensors, 6 (8). pp. 3072-3081. ISSN 2379-3694

Published by: American Chemical Society

URL: <https://doi.org/10.1016/10.1021/acssensors.1c01187>  
<<https://doi.org/10.1016/10.1021/acssensors.1c01187>>

This version was downloaded from Northumbria Research Link:  
<http://nrl.northumbria.ac.uk/id/eprint/46840/>

Northumbria University has developed Northumbria Research Link (NRL) to enable users to access the University's research output. Copyright © and moral rights for items on NRL are retained by the individual author(s) and/or other copyright owners. Single copies of full items can be reproduced, displayed or performed, and given to third parties in any format or medium for personal research or study, educational, or not-for-profit purposes without prior permission or charge, provided the authors, title and full bibliographic details are given, as well as a hyperlink and/or URL to the original metadata page. The content must not be changed in any way. Full items must not be sold commercially in any format or medium without formal permission of the copyright holder. The full policy is available online: <http://nrl.northumbria.ac.uk/policies.html>

This document may differ from the final, published version of the research and has been made available online in accordance with publisher policies. To read and/or cite from the published version of the research, please visit the publisher's website (a subscription may be required.)

# A Piezoelectric Smart Patch Operated with Machine Learning Algorithms for Effective Detection and Elimination of Condensation

Qian Zhang<sup>a,b</sup>, Yong Wang<sup>a,b,c</sup>, Tao Wang<sup>a</sup>, Dongsheng Li<sup>a</sup>, Jin Xie<sup>a,\*</sup>, Hamdi Torun<sup>b</sup>, Yongqing Fu<sup>b,a,\*</sup>

\* Corresponding authors: xiejin@zju.edu.cn; richard.fu@northumbria.ac.uk

<sup>a</sup> The State Key Laboratory of Fluid Power and Mechatronic Systems, Zhejiang University, Hangzhou 310027, China

<sup>b</sup> Faculty of Engineering and Environment, University of Northumbria, Newcastle upon Tyne NE1 8ST, UK

<sup>c</sup> Key Laboratory of 3D Micro/Nano Fabrication and Characterization of Zhejiang Province, School of Engineering, Westlake University, Hangzhou 310024, China

**KEYWORDS:** *Flexible devices, Condensation detection and elimination, Lamb waves, Random forest algorithm, Respiration detection*

---

**ABSTRACT:** Timely detection and elimination of surface condensation is crucial for diverse applications in agriculture, automotive, oil and gas industries, and respiratory monitoring. In this paper, a smart patch based on a ZnO/aluminum ( $\sim 5 \mu\text{m}/50 \mu\text{m}$  thick) flexible Lamb wave device has been proposed to detect, prevent and eliminate condensation, which can be realized using both of its surfaces. The patch is operated using a machine learning algorithm which consists of data preprocessing (feature selection and optimization) and model training by a random forest algorithm. It has been tested in six cases, and the results show good detection performance with average *Precision* = 94.40% and average *F1 score* = 93.23%. Principle of accelerating evaporation is investigated in order to understand the elimination and prevention functions for surface condensation. Results show that both dielectric heating and acousto-thermal effect have their contributions, whereas the former is found more dominant. Furthermore, the functional relationship between the evaporation rate and the input power is calibrated, showing a high linearity ( $R^2 = 97.64\%$ ) with a slope of  $\sim 3.6 \times 10^{-5} \text{ 1}/(\text{s}\cdot\text{mW})$ . With an input power of  $\sim 0.6 \text{ W}$ , the flexible device has been proven effective in the prevention of condensation.

---

Condensation is a ubiquitous phenomenon, which is common in natural and built environments with a wide range of scale from kilometer-long pipelines to biological cells [1-5]. It is quite useful in solvent recovery [6], desalination of sea water [7], sterilization [8] and respiration detection [9]. However, undesirable condensation could cause problems such as accelerating corrosion of pipelines [10], blocking the views of the windshield [11], and increasing the risk of infection of crops as a result of the growth of fungi and bacteria in the water [12]. Consequently, timely detection and elimination of condensation are of great importance for many applications. Most of the currently reported condensation detectors measure the capacitance changes caused by the changes of dielectrics (e.g., formation of dew) in order to determine whether the condensation occurs [12-16]. However, these detectors are susceptible to the variations of electrical characteristics of liquids and ambient humidity and also show a strong nonlinearity. In this paper, we propose a flexible Lamb wave device to monitor the dissipation of acoustic energy during condensation, and it can effectively not only detect but also prevent or remove the surface condensation.

Flexible piezoelectric acoustic wave devices have recently been employed in sensing [17], radio frequency (RF) wireless system [18-19], acoustofluidics [20] and lab-on-a-chip [21],

with advantages of good stability, simple fabrication, low cost, compactness and portability. Among different types of acoustic wave devices, flexible Lamb wave device (for example, with a structure of ZnO/Al ( $\sim 5 \mu\text{m}/\sim 50 \mu\text{m}$  thick) and wavelength of  $100 \mu\text{m}$ ) can excite Lamb waves by applying RF signals to the interdigital transducers (IDTs). The device is sensitive to the mass loading on both of its surfaces. As shown in Fig. 1, the small droplets condensed on the surface of the device lead to the energy dissipation of the acoustic waves, resulting in the changes of the S21 parameters. This is the fundamental basis of condensation detection. On the other hand, surface acoustic wave (SAW) devices have been proven effective in heating the droplets on their surfaces [22-23], thus this flexible device can also be used to prevent and eliminate surface condensation.

In this paper, we present a flexible smart patch based on a flexible Lamb wave device and a machine learning algorithm, which can effectively detect, prevent and eliminate surface condensation. In terms of detection, condensation is generally accompanied by variations in ambient temperature and humidity, which may lead to misjudgment. Therefore, in addition to the response of the flexible device to surface condensation, the device's responses to temperature and humidity variations are also investigated for comparisons. Furthermore, several addi

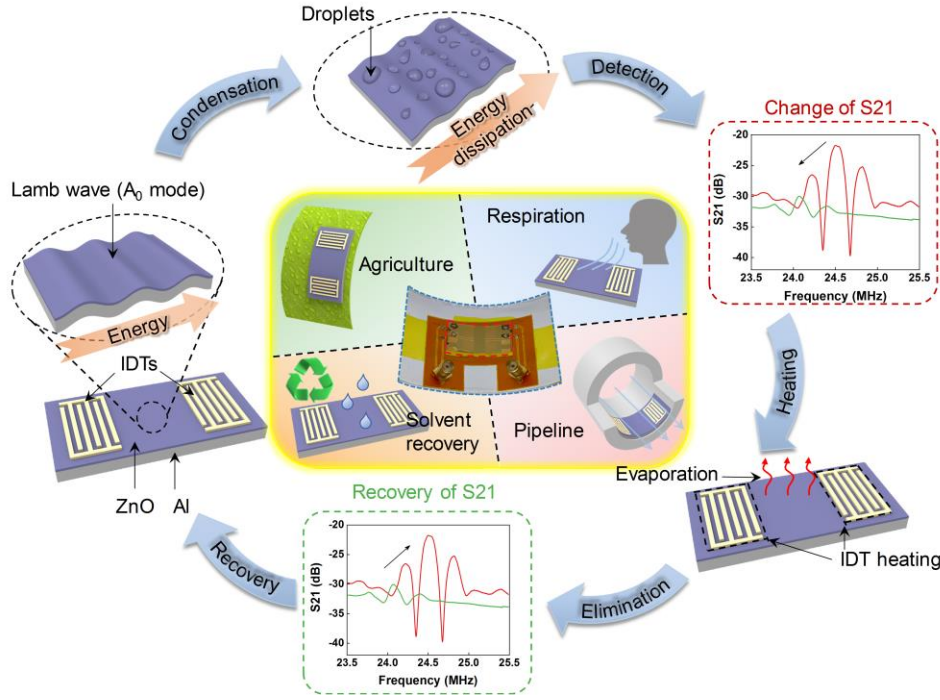


**Figure 1. Schematic illustration of the flexible acoustic wave device that detects surface condensation by analyzing the variations of S21 parameters caused by acoustic energy dissipation, and subsequently eliminates the condensation by thermal effect. The inset includes the potential applications and a photograph of the flexible device.**

-tional experiments including the condensation detection using back surface of the device, or using a bent device, and detecting different types of liquids and respiration, are conducted in order to demonstrate the broad applicability of the flexible smart patch. The principle and performance of prevention and elimination of surface condensation are studied, and the functional relationship between input power and evaporation rate is calibrated.

## Experimental

### Fabrication

Aluminum (Al) foils with a thickness of  $\sim 50 \mu\text{m}$  were used as the substrate of the flexible acoustic wave device. ZnO thin film ( $\sim 5 \mu\text{m}$  thick) was then deposited on the Al foil using magnetron sputtering technique, which can produce a film with a good orientation of c-axis (0002), as demonstrated by the X-ray diffraction (XRD) characterization in our previous work [24]. Furthermore, interdigital transducers (IDTs) with a wavelength of  $100 \mu\text{m}$  were fabricated using the standard photolithography and lift-off process, where  $80 \text{ nm}/5 \text{ nm}$  thick Au/Cr film was deposited to form the electrodes.

### Experimental setup

Fig. 2 shows the experimental setup, which can be divided into three parts: (1) generation system for condensation (cooling module and airflow generation); (2) detection system (real-time recording of S21 parameters and temperature); and (3) elimination component (high-power sinusoidal signal generation). The detection and elimination functions are not operated concurrently, but alternately by switching. In the first part (for condensation), a flexible acoustic wave device was pasted on a printed circuit board (PCB), which was placed onto a semiconductor cooler in a chamber. The humid air flow ( $\sim 100 \text{ RH}\%$ ) going through the chamber was generated by a pump ( $\sim 1.3 \text{ LPM}$ )

through a gas-washing bottle, resulting in the condensation when it encounters the cold surface of sample. In the second part (for detection), a network analyzer (Agilent E5061B) was used to measure S21 spectrum of the flexible device. A thermometer was pasted on the PCB, adjacent to the flexible device, to monitor the temperature variations in real-time. The temperature data acquisition module was used to measure the resistance of the thermometer, which was converted into temperature readings and sent to the computer through a serial port. A LabVIEW program was used to display and synchronously record the experimental results, including the S21 data collected by the network analyzer and the temperature data collected by the acquisition module. In the third part (for elimination), a sinusoidal excitation signal was

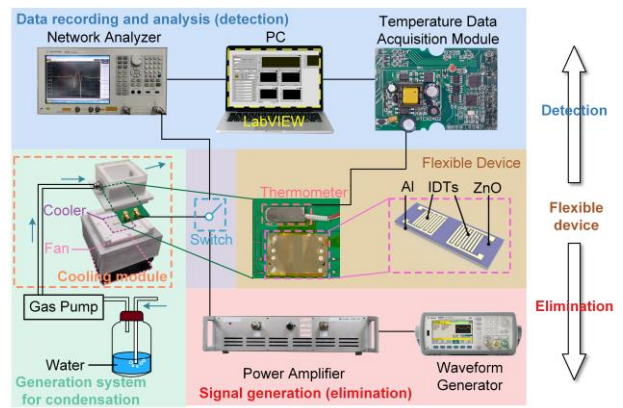


**Figure 2. The experimental setup for the flexible acoustic wave device, which can be divided into three parts according to their functionality, i.e., promoting condensation (cooling module and airflow generation), detection (recording of S21 parameters and temperature), and elimination (sinusoidal signal**

generation). The functions of detection and elimination can work alternately by switching.

generated by a waveform generator (Agilent 33522A), amplified by a power amplifier (MWPA100K, output impedance = 50  $\Omega$ ), and then applied to the IDTs.

### Design of experiments

As listed in Table 1, twelve groups of experiments, including temperature experiments (T1 to T5, 20°C to 70°C), humidity experiments (H1 to H4, ~100 RH%) and condensation experiments (C1 to C17), were designed to evaluate the detection performance of the flexible device. The temperature and humidity experiments were designed to mimic the ambient changes, where either the temperature or the humidity was changed during the experiments. The experiments of condensation were divided into 6 groups, corresponding to the cases

**Table 1. Detailed experiments design**

Temp. exp.	Condensation exp.		
T1 20-30°C	C1-C2	<b>I.</b>	Water (TS)
T2 30-40°C	C3-C5	<b>II.</b>	Ethanol (TS)
T3 40-50°C	C6-C7	<b>III.</b>	Ethyl acetate (TS)
T4 50-60°C	C8-C11	<b>IV.</b>	Water (BS)
T5 60-70°C	C12-C14	<b>V.</b>	Respiration (TS)
Humidity exp.	C15-C17	<b>VI.</b>	Bent device&Water (TS)
H1-H4	~100 RH%		

TS = Top side, BS = Back side. Ambient parameters: Temp. exp. (64 RH%); Humidity exp. (15°C); Condensation exp. (15-20°C and ~64 RH%).

of I to VI, where the tiny droplets on the device's surface were generated by condensation (cases I and IV), ultrasonic spray (cases II, III and VI) or respiration of a volunteer (case V), respectively. In addition to the general case of water condensation on the top surface (case I), we also investigated the influences of liquid types on the detection performance, including

ethanol (case II) and ethyl acetate (case III). Because the Lamb waves propagate through the entire plate thickness, there is also a normal vibration component on the back surface of the device. Similarly, water condensation on the back surface can lead to dissipation of acoustic energy which can be detected by the S21 parameter (case IV). Compared with the top surface, detection using the back surface can isolate the condensation from the IDTs and piezoelectric material (ZnO). Respiration is a more complex application (case V), where both increases of temperature and condensation occur simultaneously as soon as the flexible device encounters the hot and humid exhaled air flow. To simulate the applications under bending conditions, we taped the flexible device onto a cylindrical surface with a diameter of 9 cm and then investigated its detection performance (case VI).

## Results and discussions

### Detection of condensation

#### Shift in the resonant frequency

The resonant frequencies of Lamb wave devices shift in response to changes in temperature, which is determined by their temperature coefficient of frequency (TCF). This effect should be decoupled from the mass loading effect, which is the fundamental principle for the detection of condensation. All these effects were firstly investigated via the experiments of cooling and condensation, in order to understand the behavior of the flexible ZnO/Al device under various external stimuli. As shown in Fig. S1 in the supporting information (SI), the TCF was measured to be -452.65 ppm/°C for the  $A_0$  mode ( $R^2 = 99.10\%$ ). Fig. 3(a) shows the changes of resonant frequency and the temperature variations during the processes of cooling and then condensation. The condensation process can be divided into two stages. In stage I, the resonant frequency decreases with the gradually accumulated liquid droplets. In stage II, the acoustic

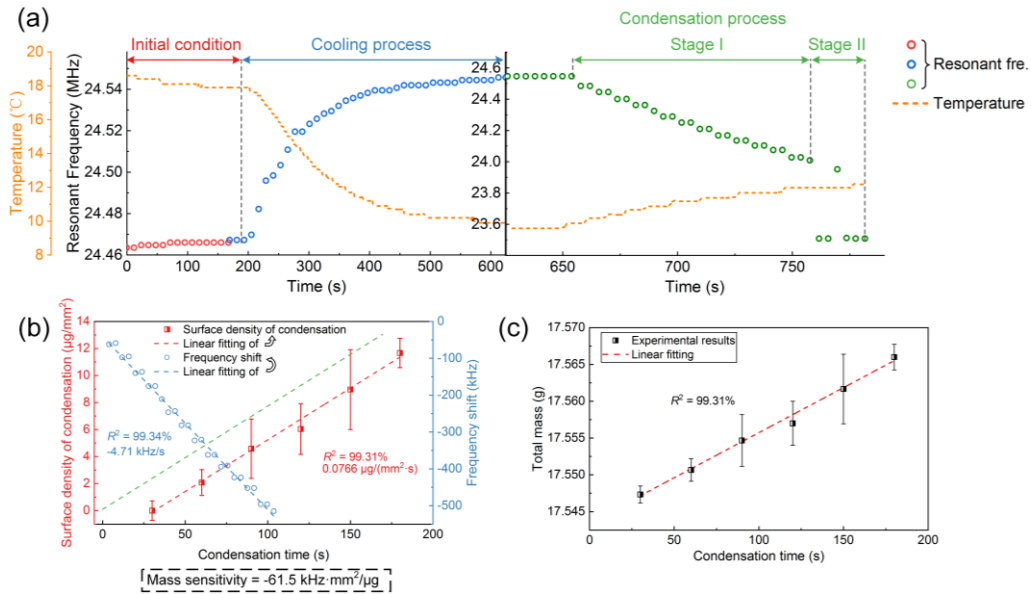


**Figure 3. (a) The resonant frequency and the temperature of the flexible device in the cooling and condensation processes. (b) The surface density of condensation and the frequency shift of the flexible device measured as a function of condensation time. The reason why the red dotted line (experimental data) does not pass through the origin may be the evaporation effect in the process of measuring**

the mass. Therefore, a green dotted line parallel to the red dotted line and passing the origin is made, which represents the estimated value. (c) The total mass of the flexible device, the printed circuit board (PCB) and the condensation. Error bars in (b) and (c) indicate the standard deviation ( $n = 3$ ).

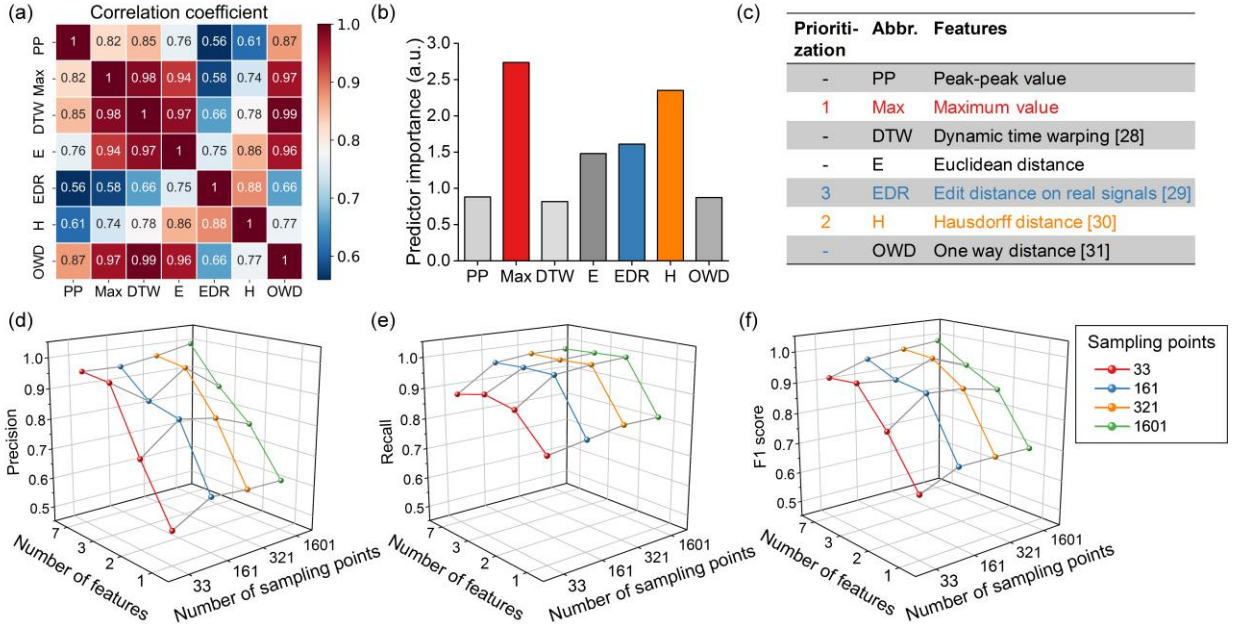


**Figure 4.** (a) The correlation coefficient matrix, (b) the estimated quantitative importance obtained by the random forest algorithm, and (c) the prioritization as well as the abbreviations of the seven selected features. The (d) Precision, (e) Recall and (f) F1 score of the prediction results using different number of features (1, 2, 3 and 7) and sampling points (33, 161, 321, 1601).

waves dissipate with accumulated liquid, leading to the disappearance of the resonant peak. Although the frequency corresponding to the maximum amplitude can be found, it is not caused by the acoustic waves. The increase of resonant frequency (~79 kHz) in the cooling process is only induced by the decrease in temperature, whereas both the mass loading and temperature rise contribute to the decrease of the resonant frequency in the stage I of condensation process, which are ~514 kHz and ~26 kHz, respectively.

As shown in Fig. 3(b), the frequency shift caused by mass loading, which can be obtained by excluding the contributions of temperature, is proportional to the condensation time ( $R^2 = 99.34\%$ ). In addition, measured by a precision balance, the mass of condensation is also linearly related to the condensation time ( $R^2 = 99.31\%$ ), as shown in Fig. 3(c). Therefore, the frequency shift is proportional to the changes of mass and surface density of condensation, assuming that the condensed droplets are uniformly distributed. The mass sensitivity is defined as  $S_{mass} = f_s \cdot A / m$ , where  $f_s$  is the frequency shift,  $A$  and  $m$  are the area and mass of the condensation, respectively. The mass sensitivity of the  $A_0$  mode of the flexible device is calculated to be -61.5 kHz·mm<sup>2</sup>/μg, as shown in Fig. 3(b). In brief, both the temperature and mass loading can lead to significant frequency shifts of the flexible device, which make it hard to determine if there is condensation on the device surface.

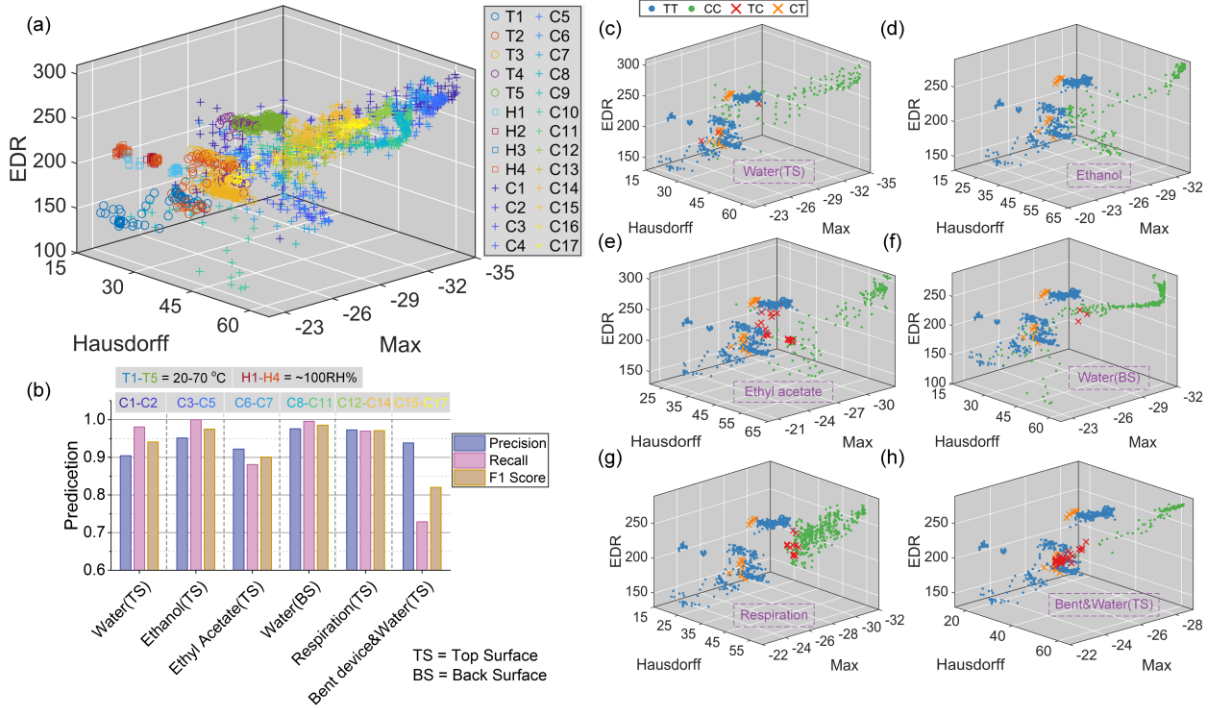
### Detection algorithm

To solve the above problem, in this section, a new method based on a random forest algorithm [25-27] is applied to identify these two stimuli. Since the mass of liquid can be infinitely close to zero, a threshold is defined, which is also the minimum detection limit. When the surface density of the liquid exceeds this threshold, it is considered that condensation has occurred. In this case, the previously mentioned problem can be assumed as a binary classification problem, i.e., to distinguish the non-

condensation (temperature change and humidity change) and condensation (mass change). In order to determine the appropriate threshold, classification preliminary tests using the following algorithm with thresholds of 0, 1.5 and 3 μg/mm<sup>2</sup> were separately conducted on a small part of the data set. The obtained results show that the algorithm can effectively identify condensation starting from 3 μg/mm<sup>2</sup>. Consequently, the threshold value of 3 μg/mm<sup>2</sup> is determined in this study. To involve more information, the S21 parameters in a frequency band (23.5-25.5 MHz) adjacent to the resonant frequency were chosen as original features. Frequency-amplitude response of S21 in this band is composed of 1601 points, which can be regarded as a 1601-dimensional vector. This method makes the classification result into a function of the selected frequency band, whose robustness will be discussed in Section 3.1.3.

As shown in Fig. 4(c), each original vector can reduce dimension by a nonlinear mapping to obtain seven shape related features, which is beneficial for simplifying calculation and preventing over fitting. Generally speaking, as the number of features increases, the classification performance first increases rapidly and then stabilizes. Too many or invalid features may also cause the degradation of classification performance. The reason for choosing only seven rather than more features is that these seven features can already achieve sufficiently good (or stabilized) classification performance. The calculation methods of the seven features are shown in the SI for more detail.

The training set, which is not shown in Table 1, is composed of experiments of temperature (20°C to 70°C), humidity (~100 RH%) and condensation (similar to the case I). For the six cases investigated in Table 1, each case has its own corresponding test set, including the common data (the temperature and humidity experiments) and the data in the corresponding condensation experiment (one of case I to VI). The detailed random forest algorithm and calculation process are shown in the SI. A MATLAB program was used for data preprocessing, model



training, prediction and visualization. The results of classification are evaluated by *Precision*, *Recall* and *F1 score*, which are

**Figure 5. (a) The whole test set mapped to a selected 3-D space with coordinates of Maximum value, Hausdorff distance and EDR, which is equivalent to data preprocessing for dimension reduction. (b) The prediction results of the classification model obtained by the random forest algorithm on the six test sets corresponding to the six cases. The visualization of classification results on the six test sets, corresponding to the cases of (c) water on top side, (d) ethanol, (e) ethyl acetate, (f) water on back side, (g) respiration and (h) bent device, respectively.**

shown in Eq. (1). The first letter denotes the predicted result and the latter one denotes the actual case. This generates four combinations (i.e., *CC*, *CT*, *TC*, *TT*), where *C* represents condensation and *T* represents no condensation.

$$\begin{aligned}
 Precision &= \frac{CC}{CC + CT}, Recall = \frac{CC}{CC + TC}, \\
 F1 &= \frac{Precision \times Recall}{Precision + Recall}
 \end{aligned} \quad (1)$$

As is well known, the different features do not contribute equally to the classification and some of the features may be highly correlated to each other, which leads to redundant features. Less features and sampling points are preferred on the premise of not significantly reducing the prediction performance. To find and eliminate redundant features, the data set corresponding to the case I was used for the following calculation and analysis, as shown in Fig. 4. The correlation coefficient matrix (as shown in Fig. 4(a)), together with the estimated importance of the features (as shown in Fig. 4(b)) obtained by the random forest algorithm [27], were used to determine the priority of features (as shown in Fig. 4(c)). The *Precision*, *Recall* and *F1 score* shown in Figs. 4(d) to 4(f) indicate the prediction performances of the device when different number of features (1, 2, 3 and 7) and sampling points (33, 161, 321, 1601) are adopted. The features are selected according to the priority shown in Fig. 4(c) when the number of features is 1, 2 or 3. It was found that single feature can provide only limited performance in prediction (*Precision* = 61.95%, *Recall* = 82.46%, *F1* = 70.75%) using 321 sampling points, whereas it was

commonly used in binary classification problems, as

significantly improved (*Precision* = 95.56%, *Recall* = 98.05%, *F1* = 96.79%) by adding two more features. It was also found that adding features can effectively make up for the lack of sampling points. For example, using 7 features and only 33 sampling points, the *F1 score* is still larger than 90%. Based on the above analysis, three features and 321 sampling points will be used in the subsequent data processing for high classification performance (*F1 score* > 95%) and ease of visualization (number of features  $\leq 3$ ).

### Condensation detection for various applications

In this section, the performance of the proposed method for detecting surface condensation in six different cases is discussed. Based on the method proposed in the Section 3.1.2, the data sets including a total of 5065 points listed in the Table 1 are mapped into a 3-D space with coordinates of Maximum value, Hausdorff distance and EDR (edit distance on real sequence), as shown in Fig. 5(a). After the dimension reduction of the raw S21 data, the classification model can be obtained by using the random forest algorithm and the training set, which was subsequently verified by the test sets corresponding to the six cases. The *Precision*, *Recall* and *F1 score* were then calculated by comparing the predicted results with the actual ones, as shown in Fig. 5(b). The proposed method performed well in the experiments of water (TS), ethanol (TS), water (BS) and respiration (TS), where the *Precision*, *Recall* and *F1 score* are all above 90%. Although the *Precision* was very high (92.16% and 93.83%) in the experiments of ethyl acetate (TS) and bent device (TS), the *Recall* was decreased significantly (88.1% and 72.87%), resulting in the decrease of the *F1 score* (90.09% and

82.03%). In practice, it is attractive to build a single model applicable for different applications without additional calibration, which is possible for the flexible device. Therefore, in order to simulate the unknown working conditions, the data of condensation experiments included in the training set are only the general conditions (case I). In other words, the other five experiments are unknown for the trained model, which is one of the reasons accounting for the inconsistent classification performance in different experiments. Nevertheless, the model still shows good classification ability for the unknown but similar experiments, indicating that the model is applicable at the cost of a possible reduction in prediction performance.

Figs. 5(c) to 5(h) show the visualized classification results corresponding to the 6 various cases. The data points in each case can be divided into two distinct clusters in the 3-D space, in which the points in the temperature experiments are distributed in the lower left, the points in the condensation experiments are distributed in the upper right, and the misclassified points are mainly concentrated at the boundary of these two clusters. Due to the different properties of the surface liquid and the bending condition of the device, the spatial distributions of the points in the six experiments are not exactly the same, as shown in Figs. 5(c) to 5(h), which is ultimately manifested as the difference in the classification performance of the model from the different test sets.

The influence of selection of frequency band on classification results was also investigated by using five different frequency bands, each of which includes at least the main resonance peak and its adjacent side lobes. The sampling intervals were all set to 62.5 kHz in all the frequency bands. As shown in Fig. S3, the classification results obtained by applying the five different frequency bands have comparable *FI scores* (average standard deviation = ~2% for the six cases), indicating the robustness of the algorithm. The variations of the S21 parameters are mainly caused by the change of the resonance peak and its adjacent side lobes, and the data in other frequency band have little influences on the classification results, which can be regarded as noise. Therefore, the main resonance peak and its adjacent side lobes must be included in the frequency band, whereas no strict requirement is presented for the selection of the frequency range. In addition, the preprocessing of the original data (the calculation of the seven features) is also helpful for enhancing robustness, since most of these features are kindly tolerant of noise in data.

In summary, in order to detect surface condensation and eliminate the false responses caused by temperature and humidity, a new method based on the S21 parameters in the frequency band is adopted, which shows a good recognition performance even under certain unknown though similar conditions (cases II to VI).

### Condensation evaporation

In addition to detecting the condensation on the surface, the flexible device can also be used to accelerate the removal or evaporation of droplets on surface. Its principle and performance are investigated in this section. There are two possible causes accounting for the accelerated evaporation of droplets: leaky acoustic waves and dielectric heating [23]. The leaky acoustic waves interacting with the surface droplets can induce internal streaming in liquid, the energy of which can be converted into heat, i.e., the acoustothermal effect [22]. The principle of dielectric heating is that the electric dipoles are subjected to a time-varying moment in an alternating electric field, resulting in rotation of the dipoles and thus the increase of their

average kinetic energy, which is reflected in the rise of temperature from a macroscopic perspective. The power of the dielectric heating is given by [32]:

$$P = \omega \epsilon_0 \epsilon_r'' |E|^2 \quad (2)$$

where  $P$  is the heating power density,  $\omega$  and  $E$  are respectively the angular frequency and strength of the electric field,  $\epsilon_0$  is the permittivity of vacuum and  $\epsilon_r''$  is the loss factor (the imaginary part of the relative permittivity) of ZnO.

In order to reveal which of these two factors is the dominant, four excitation frequencies were selected, i.e., 24.4 MHz, 24.5 MHz, 24.9 MHz and 25.3 MHz, as shown in Fig. 6(b). According to the Eq. (2), the dielectric heating powers are similar for these four excitation frequencies, which is also illustrated by the equilibrium surface temperature as shown in Fig. 6(a). The equilibrium surface temperature refers to the temperature of the flexible acoustic wave device on top surface in a steady state when excited by a sinusoidal power supply with an output impedance of 50  $\Omega$  and voltage of 31.6 V<sub>pp</sub> at room temperature of 18.5°C. This surface temperature, determined by the dielectric heating power, was recorded using an infrared thermometer (Smart Sensor AT380). Nevertheless, the choice of the excitation frequency has also a great influence on the intensity of the excited acoustic wave. According to the  $\delta$ -function

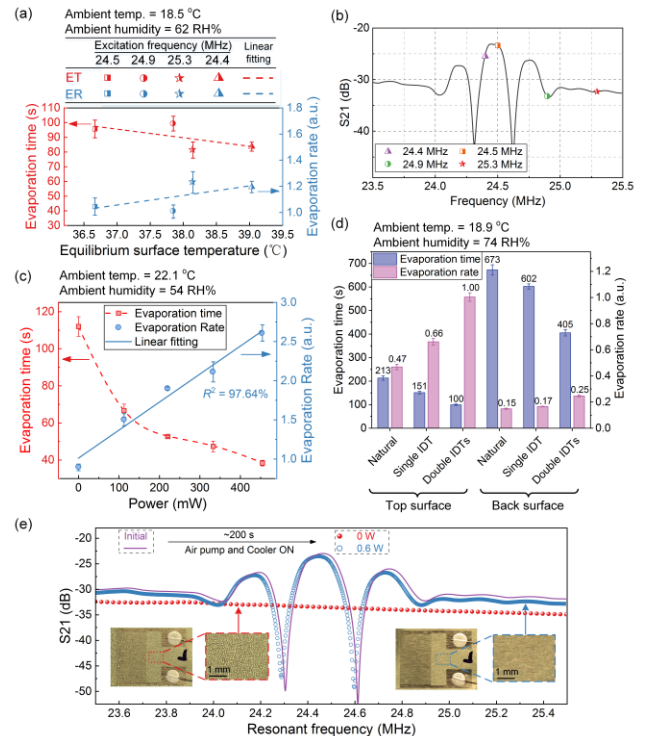


**Figure 6.** (a) Evaporation time, evaporation rate and equilibrium surface temperature of the flexible device when excited by 4 sinusoidal signals with different frequencies (24.4 MHz, 24.5 MHz, 24.9 MHz and 25.3 MHz), the position of which in the S21 curve is shown in (b). The evaporation rate is defined as 100 times the reciprocal of the evaporation time. The equilibrium surface temperature refers to the steady temperature of the top surface without liquid applied when the flexible device is excited by a sinusoidal power source with an output impedance of 50  $\Omega$  and peak value of 15.8 V at an ambient temperature of 18.5°C. (c) The functional relationship of evaporation time/rate and input power in the range of 0 to ~0.45 W. (d) Comparing the evaporation performance of the top surface and the back surface by experiments of natural evaporation, single

**and double IDTs heating. (e) After condensed for ~200 s, the S21 parameters and photographs of the flexible device with an input power of 0 W and ~0.6 W respectively. Error bars in this Figure indicate the standard deviation (n = 3).**

model [33], each edge of the interdigital electrode can be regarded as an acoustic source and the excited plane waves at coordinate  $x$  is a superposition of a series of waves, the amplitude of which ( $A_p$ ) takes the form [33]:

$$A_p \propto \left| \sum_{n=1}^N \exp \left[ i \frac{2\pi f}{v} (x_n - x) \right] \right| \quad (3)$$

where  $f$  is the excitation frequency,  $v$  is the plane wave velocity,  $x_n$  and  $N$  are the coordinates and number of the acoustic sources. It can be proven that the  $N$  acoustic waves will cancel each other with an excitation frequency far from the resonant frequency (i.e., group A, 24.9 MHz and 25.3 MHz). On the contrary, they will superpose in a same phase to generate a strong acoustic wave (i.e., group B, 24.4 MHz and 24.5 MHz). Evaporation time is defined as the time required for complete evaporation of the droplets on surface, and the total mass of the droplets can be adjusted by the time of condensation, as shown in Fig. 3(c). In this paper, the time of condensation is set to be 3 minutes to keep the mass of droplets consistent in each experiment. On this basis, the evaporation rate is proportional to the reciprocal of the evaporation time. As shown in Fig. 6(a), the linear fitting indicates that the evaporation rate increases with the temperature. However, the evaporation rates of the group B (24.4 MHz and 24.5 MHz) do not show obvious superior performance comparing to those of the group A (24.9 MHz and 25.3 MHz), indicating that the dielectric heating might be dominant in accelerating evaporation. The excitation frequency of 25.3 MHz was adopted in the subsequent experiments due to its best performance in the evaporation experiments.

In addition, similar experiments investigating the evaporation time of a single deionized water droplet (~1  $\mu$ L) were carried out when the four excitation frequencies were used, and the results are shown in Fig. S2. The droplets were manually dropped at the center of the device's surface, and each experiment was repeated for three times. As shown in Fig. S2(a), comparing to natural evaporation, the evaporation time is significantly shortened for ~591 s with only dielectric heating (group A). However, the evaporation time is further shortened by only ~3.5 s when using the excitation frequencies in group B. In order to investigate the contribution of the acoustic waves, evaporation time is drawn as a function of the equilibrium temperature of the flexible device, and the results shown in Fig. S2(b). The linear fitting result indicates the contribution of dielectric heating in the temperature range of 36.5°C to 39°C. Subsequently, the offsets of evaporation time deviated from the fitting line are calculated, which represent the contribution of the acoustic waves, as shown in Fig. S2(c). It is found that the group B performs better than the group A, which shows that the acoustic waves also contribute to evaporation but less effective comparing to dielectric heating for this 50  $\mu$ m thick flexible device.

Furthermore, the influence of the input power on the evaporation rate has been also studied. In the range of 0 to 450 mW, the input power is approximately and inversely proportional to the evaporation time, and linearly related to the evaporation rate ( $R^2 = 97.64\%$ ), as shown in Fig. 6(c). Fig. 6(d) shows a comparison of evaporation rates on top and back surfaces of the device. With an input power of ~33 mW, the evaporation of droplets on the back surface can be accelerated, which is similar to the result at the top surface. However, due to the difference of

surface properties and wave amplitude, the evaporation rate on the back surface is only 1/4 to 1/3 of that on the top surface. In addition to accelerating the evaporation of droplets, thermal effect can effectively prevent surface condensation. With the input power of 0 W and 0.6 W, respectively, the flexible device was placed in the environment of Fig. 3(a) for 200 s, and then its surface was observed and the S21 parameters were measured. As shown in Fig. 6(e), the surface of the device is covered with dense droplets when the input power is zero, whereas no visible droplets can be found in the case of 0.6 W input power. This has also been demonstrated from the changes of S21 parameters.

## Conclusions

In summary, through the carefully designed experiments, the capabilities of the proposed smart patch to detect and eliminate surface condensation have been investigated under various conditions. The patch has been operated using a machine learning algorithm to distinguish effective response (condensation) from false response (temperature and humidity variations). The algorithm is based on a classifier that was trained using a random forest algorithm and the S21 data after nonlinear dimensionality reduction, which performed well in six different test sets (average *Precision* = 94.40% and average *F1 score* = 93.23%). The flexible device has been shown effectively to prevent and eliminate the surface condensation with an input power of a few tenths of a watt at a frequency of ~25.3 MHz, and the evaporation rate is approximately linearly related to the input power ( $R^2 = 97.64\%$ ). In the experimental environment, the evaporation rate was increased up to ~3 times with an input power of ~0.45 W compared to that under natural condition. In addition, we have shown that dielectric heating could be the main reason to prevent and eliminate surface condensation for the flexible ZnO/Al (~5  $\mu$ m/~50  $\mu$ m) device, although the acoustothermal effect also has a contribution. Our work demonstrates the promising prospect of proposed smart patch in broad applications including respiration detection, agricultural environmental monitoring, pipeline corrosion protection and automotive industry.

## ASSOCIATED CONTENT

### Supporting Information.

Temperature sensitivity (TCF) of the flexible device (Figure S1); evaporation time of a single deionized water droplet (~1  $\mu$ L) when the flexible device is excited by four different frequencies (Figure S2); investigation of robustness on the frequency band selection (Figure S3); calculation method of the seven features; training method of the random forest classifier. This material is available free of charge via the Internet at <http://pubs.acs.org>.

## AUTHOR INFORMATION

### Notes

The authors declare no competing financial interest.

## ACKNOWLEDGMENT

This work was supported by the National Natural Science Foundation of China under Grant 51875521, the Zhejiang Provincial Natural Science Foundation of China under Grant LZ19E050002, the Engineering Physics and Science Research Council of UK (EPSRC EP/P018998/1) and UK Fluidic Network (EP/N032861/1) Special Interest Group of Acoustofluidics, International Exchange Grant (IEC/NSFC/201078) through Royal Society and the National NSFC.

## REFERENCES

[1] Cha, H.; Vahabi, H.; Wu, A.; Chavan, S.; Kim, M.-K.; Sett, S.; Bosch, S. A.; Wang, W.; Kota, A. K.; Miljkovic, N. Dropwise Condensation on Solid Hydrophilic Surfaces. *Sci. Adv.* **2020**, *6* (2), eaax0746.

[2] Yang, Q.; Sun, P. Z.; Fumagalli, L.; Stebunov, Y. V.; Haigh, S. J.; Zhou, Z. W.; Grigorieva, I. V.; Wang, F. C.; Geim, A. K. Capillary Condensation under Atomic-Scale Confinement. *Nature* **2020**, *588* (7837), 250–253.

[3] Shin, Y.; Brangwynne, C. P. Liquid Phase Condensation in Cell Physiology and Disease. *Science* **2017**, *357* (6357), eaaf4382.

[4] Hou, Y.; Yu, M.; Chen, X.; Wang, Z.; Yao, S. Recurrent Filmwise and Dropwise Condensation on a Beetle Mimetic Surface. *ACS Nano* **2015**, *9* (1), 71–81.

[5] Wen, R.; Li, Q.; Wu, J.; Wu, G.; Wang, W.; Chen, Y.; Ma, X.; Zhao, D.; Yang, R. Hydrophobic Copper Nanowires for Enhancing Condensation Heat Transfer. *Nano Energy* **2017**, *33*, 177–183.

[6] Henning, K. Solvent Recycling, Removal, and Degradation. *Handb. Solvents* **2019**, 1635–1727.

[7] Fujiwara, M.; Takahashi, K.; Takagi, K. Improvement of Condensation Step of Water Vapor in Solar Desalination of Seawater and the Development of Three-Ply Membrane System. *Desalination* **2021**, *508*, 115051.

[8] Hall, L.; Otter, J. A.; Chewins, J.; Wengenack, N. L. Use of Hydrogen Peroxide Vapor for Deactivation of Mycobacterium Tuberculosis in a Biological Safety Cabinet and a Room. *J. Clin. Microbiol.* **2007**, *45* (3), 810–815.

[9] Janik, P.; Janik, M. A.; Wróbel, Z. Micro-Condensation Sensor for Monitoring Respiratory Rate and Breath Strength. *Sensors Actuators, A Phys.* **2012**, *185*, 160–167.

[10] Li, Y.; Yan, M.; Zhang, L.; Chen, G.; Cui, L.; Song, Z.; Chang, J.; Ma, C. Method of Flash Evaporation and Condensation - Heat Pump for Deep Cooling of Coal-Fired Power Plant Flue Gas: Latent Heat and Water Recovery. *Appl. Energy* **2016**, *172*, 107–117.

[11] Gould, D.; Meiners, M.; Benecke, W.; Lang, W. Condensation Detection Using a Wirelessly Powered RF-Temperature Sensor. *IEEE Trans. Veh. Technol.* **2009**, *58* (4), 1667–1672.

[12] Wei, Y. Q.; Bailey, B. J.; Stenning, B. C. A Wetness Sensor for Detecting Condensation on Tomato Plants in Greenhouses. *J. Agric. Eng. Res.* **1995**, *61* (3), 197–204.

[13] Dumitru, V.; Costea, S.; Brezeanu, M.; Stan, G. E.; Besleaga, C.; Galca, A. C.; Ionescu, G.; Ionescu, O. InN Based Water Condensation Sensors on Glass and Flexible Plastic Substrates. *Sensors (Switzerland)* **2013**, *13* (12), 16940–16949.

[14] Kubota, Y.; Mishra, V. L.; Ando, T.; Sakamoto, Y.; Kawakita, J. Micro/Nano Galvanic-Coupled Arrays for Early and Initial Detection and Prediction of Dew Condensation. *Sensors Actuators, A Phys.* **2020**, *303*, 111838.

[15] Karuppuswami, S.; Wiwatcharagoses, N.; Kaur, A.; Chahal, P. Capillary Condensation Based Wireless Volatile Molecular Sensor. *Proc. - Electron. Components Technol. Conf.* **2017**, 1455–1460.

[16] Oprea, A.; Bărsan, N.; Weimar, U.; Bauersfeld, M.-L.; Ebling, D.; Wöllenstein, J. Capacitive Humidity Sensors on Flexible RFID Labels. *Sensors Actuators B Chem.* **2008**, *132* (2), 404–410.

[17] Lamanna, L.; Rizzi, F.; Bhethanabotla, V. R.; De Vittorio, M. Conformable Surface Acoustic Wave Biosensor for E-Coli Fabricated on PEN Plastic Film. *Biosens. Bioelectron.* **2020**, *163*, 112164.

[18] Jiang, Y.; Zhao, Y.; Zhang, L.; Liu, B.; Li, Q.; Zhang, M.; Pang, W. Flexible Film Bulk Acoustic Wave Filters toward Radiofrequency Wireless Communication. *Small* **2018**, *14* (20).

[19] Zhou, C.; Shu, Y.; Yang, Y.; Jin, H.; Dong, S. R.; Chan, M.; Ren, T. L. Flexible Structured High-Frequency Film Bulk Acoustic Resonator for Flexible Wireless Electronics. *J. Micromechanics Microengineering* **2015**, *25* (5), 55003.

[20] Tao, R.; Mchale, G.; Reboud, J.; Cooper, J. M.; Torun, H.; Luo, J. T.; Luo, J.; Yang, X.; Zhou, J.; Canyelles-Pericas, P.; Wu, Q.; Fu, Y. Hierarchical Nanotexturing Enables Acoustofluidics on Slippery yet Sticky, Flexible Surfaces. *Nano Lett.* **2020**, *20* (5), 3263–3270.

[21] Tao, R.; Reboud, J.; Torun, H.; McHale, G.; Dodd, L. E.; Wu, Q.; Tao, K.; Yang, X.; Luo, J. T.; Todryk, S.; Fu, Y. Integrating Microfluidics and Biosensing on a Single Flexible Acoustic Device Using Hybrid Modes. *Lab Chip* **2020**, *20* (5), 1002–1011.

[22] Wang, Y.; Zhang, Q.; Tao, R.; Chen, D.; Xie, J.; Torun, H.; Dodd, L. E.; Luo, J.; Fu, C.; Vernon, J.; Canyelles-Pericas, P.; Binns,

R.; Fu, Y. A Rapid and Controllable Acoustothermal Microheater Using Thin Film Surface Acoustic Waves. *Sensors Actuators, A Phys.* **2021**, *318*, 112508.

[23] Kondoh, J.; Shimizu, N.; Matsui, Y.; Sugimoto, M.; Shiokawa, S. Development of Temperature-Control System for Liquid Droplet Using Surface Acoustic Wave Devices. *Sensors Actuators, A Phys.* **2009**, *149* (2), 292–297.

[24] Wang, Y.; Zhang, Q.; Tao, R.; Xie, J.; Canyelles-Pericas, P.; Torun, H.; Reboud, J.; McHale, G.; Dodd, L. E.; Yang, X.; *et al.* Flexible/Bendable Acoustofluidics Based on Thin-Film Surface Acoustic Waves on Thin Aluminum Sheets. *ACS Appl. Mater. Interfaces* **2021**, *13* (14), 16978–16986.

[25] Breiman, L. Random Forests. *Mach. Learn.* **2001**, *45* (1), 5–32.

[26] Biau, G.; Scornet, E. A Random Forest Guided Tour. *Test* **2016**, *25* (2), 197–227.

[27] Liaw, A.; Wiener, M. Classification and Regression by RandomForest. *R news* **2002**, *2*, 18–22.

[28] Berndt, D.; Clifford, J. Using Dynamic Time Warping to Find Patterns in Time Series. *Work. Knowl. Knowl. Discov. Databases* **1994**, *398*, 359–370.

[29] Chen, L.; Özsu, M. T.; Oria, V. Robust and Fast Similarity Search for Moving Object Trajectories. *Proc. ACM SIGMOD Int. Conf. Manag. Data* **2005**, 491–502.

[30] Huttenlocher, D. P.; Rucklidge, W. J.; Klanderma, G. A. Comparing Images Using the Hausdorff Distance under Translation. *Proc. IEEE Comput. Soc. Conf. Comput. Vis. Pattern Recognit.* **1992**, *1992-June* (9), 654–656.

[31] Lin, B.; Su, J. One Way Distance: For Shape Based Similarity Search of Moving Object Trajectories. *Geoinformatica* **2008**, *12* (2), 117–142.

[32] Issadore, D.; Humphry, K. J.; Brown, K. A.; Sandberg, L.; Weitz, D. A.; Westervelt, R. M. Microwave Dielectric Heating of Drops in Microfluidic Devices. *Lab Chip* **2009**, *9* (12), 1701–1706.

[33] Tancrèll, R. H.; Holland, M. G. Acoustic Surface Wave Filters. *Proc. - IEEE Ultrason. Symp.* **1970**, *1970-October* (3), 48–64.

